

FORMATION OF MINIGALAXIES IN DEFUNCT COSMOLOGICAL H II REGIONS

SERGEY MASHCHENKO, H. M. P. COUCHMAN, AND ALISON SILLS

Department of Physics and Astronomy, McMaster University, Hamilton, ON L8S 4M1, Canada;
syam@physics.mcmaster.ca, couchman@physics.mcmaster.ca, asills@physics.mcmaster.ca

Received 2005 September 26; accepted 2005 November 10

ABSTRACT

Using a large set of high-resolution numerical simulations incorporating nonequilibrium molecular hydrogen chemistry and a constant source of external radiation, we study gas collapse in previously photoionized minigalaxies with virial temperatures less than 10^4 K in the early universe (redshifts $z = 10$ – 20). We confirm that the mechanism of positive feedback of ionizing radiation on star formation in minigalaxies proposed by Ricotti and coworkers can be efficient despite a significant flux of metagalactic photodissociating radiation. We derive critical fluxes for the Lyman-Werner background radiation sufficient to prevent the collapse of gas in minigalaxies as a function of the virial mass of the halo and redshift. In our model, the formation of minigalaxies in defunct H II regions is most efficient at large redshifts ($z \gtrsim 15$) and/or for large local gas overdensity $\delta \gtrsim 10$. We show that nonequilibrium chemistry plays an important dynamical role not only during the initial evolutionary phase, leading to the gas becoming gravitationally unstable inside the minihalo, but also at the advanced stages of the core collapse, resulting in efficient gas accretion in the core region. We speculate on a possible connection between our objects and metal-poor globular clusters and dwarf spheroidal galaxies.

Subject headings: astrochemistry — early universe — galaxies: dwarf — galaxies: formation — methods: n -body simulations

1. INTRODUCTION

The formation of the first (small) galaxies in hierarchical cold dark matter (CDM) cosmologies has been a subject of intensive research. Both noncosmological (e.g., Tegmark et al. 1997; Fuller & Couchman 2000; Bromm et al. 2002) and cosmological (e.g., Abel et al. 1998, 2002; Yoshida et al. 2003) approaches produced a consistent picture of first stars in the universe forming inside minihalos with virial masses $\lesssim 10^6 M_\odot$ at redshifts $\gtrsim 20$. As the virial temperature of such small halos is below 10^4 K, rendering the atomic hydrogen line cooling inefficient, the primary coolant responsible for the collapse of the zero-metallicity gas is molecular hydrogen.

Haiman et al. (2000) argued that soon after the very first stars in the universe are born in rare 3 – 4σ peaks, the Lyman-Werner photons produced by these stars dissociate molecular hydrogen, making further small galaxy formation impossible. As a result, the main bulk of stars in the early universe should have formed later, when more massive galaxies with $T_{\text{vir}} > 10^4$ K, capable of cooling through atomic hydrogen lines, are formed. Cosmological simulations of Machacek et al. (2001) and Yoshida et al. (2003) corroborated the above picture by showing that even small flux $F \sim 10^{-23}$ ergs s $^{-1}$ cm $^{-2}$ Hz $^{-1}$ sr $^{-1}$ of the Lyman-Werner radiation is sufficient to suppress the formation of minigalaxies in the early universe.

Ricotti et al. (2002) demonstrated that to gain better understanding of early star formation in the universe, one has to use cosmological simulations with full radiative transfer. They uncovered an important mechanism of positive feedback of ionizing radiation from first stars on subsequent star formation in minigalaxies. In their simulations, cosmological H II regions formed around the first minigalaxies in dense filaments become sites of intense H $_2$ production after the source of the ionizing radiation is turned off. In the defunct cosmological H II regions gas cools and recombines at the same time, resulting in enhanced nonequilibrium ionization fraction and, as a consequence, increased produc-

tion of molecular hydrogen. In the model of Ricotti et al. (2002) the flux of the background Lyman-Werner radiation is calculated self-consistently by performing full radiative transfer from the sources of radiation (star-forming regions) inside the computational volume. The authors showed that the significant flux of H $_2$ photodissociating radiation does not prevent minigalaxies from being formed in and around cosmological H II regions.

From Figure 7 of Ricotti et al. (2002) and the corresponding mpeg animation in the electronic edition of the publication one can see some details of the above process. In this figure, a minigalaxy is seen to form first stars at $z \lesssim 17$ and then to undergo a few consecutive starbursts due to positive feedback of the ionizing radiation. As one can see from this figure, the minigalaxy is located inside a relatively dense cosmological filament. The temperature inside the H II regions is close to the canonical value of $\sim 10^4$ K.

More recently, O’Shea et al. (2005) presented their simulations of the formation of a primordial star within a region ionized by an earlier nearby star. These semicosmological simulations confirmed the results of Ricotti et al. (2002) by showing that there is a positive feedback due to photoionization on subsequent star formation in minigalaxies.

Cosmological simulations with full radiative transfer, such as those of Ricotti et al. (2002), are very computationally expensive, as one has to achieve both high resolution (to resolve collapsed gas in minigalaxies) and large spatial coverage (to have the rare sources of ionizing and Lyman-Werner radiation included in the computational box and to beat the cosmic variance). Instead, in this paper we use noncosmological high-resolution simulations to investigate the mechanism of positive feedback of ionizing radiation on star formation in minigalaxies in greater detail. We model both nonequilibrium chemistry and the impact of the external photodissociating radiation on collapse of gas in minigalaxies inside defunct cosmological H II regions at redshifts 20 – 10 . We confirm the result of Ricotti et al. (2002) that the positive feedback is efficient even for relatively large fluxes of

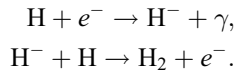
external Lyman-Werner radiation with $F \gtrsim 10^{-21}$ ergs s⁻¹ cm⁻² Hz⁻¹ sr⁻¹.

2. MODEL

Our goal is to simulate the evolution of a small, fully photoionized portion of a dense cosmological filament containing one minihalo in the early universe ($z \geq 10$) after the source of the ionizing radiation is turned off. The gas remains exposed to the external source of radiation with the photon energies below 13.6 eV (which includes Lyman-Werner photons capable of dissociating the molecular hydrogen). We assume the gas to be optically thin. To run the simulations, we use an adaptive-mesh P³M-SPH code Hydra¹ (Couchman et al. 1995). We use the scalar version 4.0 of the code, with the molecular hydrogen chemistry module developed by Fuller & Couchman (2000).

2.1. Chemistry

Molecular hydrogen is the primary coolant in the gas of primordial composition inside small dark matter (DM) halos with virial temperature less than 10⁴ K. In the primordial dust-free gas molecular hydrogen can be produced through two main channels: H₂⁺ channel and H⁻ channel. In our analysis, we consider only the latter channel, as it is known to be the dominant one at redshifts $z < 200$. In the H⁻ channel, the electron acts as a catalyst:



At the temperatures considered here ($T \leq 10^4$ K) helium is neutral. As a result, we only have to follow the evolution of five different species: H, e⁻, H⁺, H⁻, and H₂. We use all 13 major chemical reactions involving these species from the compilation of Abel et al. (1997). The reactions are listed in Table 1. We keep the reaction numeration of Abel et al. (1997). Most of the reaction rates are from Abel et al. (1997), with two exceptions: (1) for reaction 7, we use a simpler expression from Hutchins (1976), which is the way this reaction is implemented in the publicly available FORTRAN routine on Tom Abel's primordial gas chemistry page:²

$$k_7 = 1.83 \times 10^{-18} T^{0.8779} \text{ s}^{-1}, \quad (1)$$

where T is the gas temperature in K; and (2) for the photodetachment cross section of H⁻ (reaction 23) we used our own (higher quality) fitting formula to the original data of Wishart (1979) tabulated for photon energies 0.76–9.9 eV. More specifically, instead of the fitting formula $\sigma_{23} = 7.928 \times 10^5 (\nu - \nu_0)^{1.5} \nu^{-3} \text{ cm}^2$ of Abel et al. (1997), we used the following one:

$$\sigma_{23} = 2.241 \times 10^7 (\nu - \nu_0)^{1.5} \nu^{-3.1} \text{ cm}^2. \quad (2)$$

Here frequencies are in Hz. Both expressions are valid for $h\nu > h\nu_0 = 0.755$ eV. The standard and maximum deviations of our fit from the data of Wishart (1979) are 0.007 and 0.04 dex, respectively, which is much better than for the original fit (0.03 and 0.07 dex, respectively).

TABLE 1
REACTIONS

NN	Reaction	Rate Reference
1.....	H + e ⁻ → H ⁺ + 2e ⁻	1
2.....	H ⁺ + e ⁻ → H + γ	1
7.....	H + e ⁻ → H ⁻ + γ	2
8.....	H + H ⁻ → H ₂ + e ⁻	1
11.....	H ₂ + H ⁺ → H ₂ ⁺ + H	1
12.....	H ₂ + e ⁻ → 2H + e ⁻	1
13.....	H ₂ + H → 3H	1
14.....	H ⁻ + e ⁻ → H + 2e ⁻	1
15.....	H ⁻ + H → 2H + e ⁻	1
16.....	H ⁻ + H ⁺ → 2H	1
17.....	H ⁻ + H ⁺ → H ₂ ⁺ + e ⁻	1
23.....	H ⁻ + γ → H + e ⁻	3
27.....	H ₂ + γ → H ₂ ⁺ → 2H	1

NOTE.—Reaction numeration is from Abel et al. (1997).

REFERENCES.—(1) Abel et al. 1997; (2) Hutchins 1976; (3) this work.

The external source of nonionizing radiation is considered to have a power-law spectrum:

$$F_{21} = F_{\bar{\nu}} \left(\frac{\nu}{\bar{\nu}} \right)^\alpha 10^{21}, \quad (3)$$

where $F_{\bar{\nu}}$ is the radiation flux in ergs s⁻¹ cm⁻² sr⁻¹ Hz⁻¹ at the average Lyman-Werner frequency with $h\bar{\nu} = 12.87$ eV. The rate for reaction 23 can be obtained from

$$k_{23} = 4\pi \int_{\nu_0}^{\nu_L} \frac{F_{21}(\nu) 10^{-21} \sigma_{23}(\nu)}{h\nu} d\nu \text{ s}^{-1}. \quad (4)$$

Here $h\nu_L = 13.6$ eV is the hydrogen photoionization energy. We consider a steep external radiation spectrum with $\alpha = -1$. The rate equation is derived by numerically solving the integral in equation (4) with $\sigma_{23}(\nu)$ given by equation (2):

$$k_{23} = 7.465 \times 10^{-10} F_{21} \text{ s}^{-1}. \quad (5)$$

The rate for reaction 27 is

$$k_{27} = 1.382 \times 10^{-12} F_{21} \text{ s}^{-1} \quad (6)$$

(Abel et al. 1997).

For a species A , we express the fractional abundance f_A in terms of the proton number density n of all hydrogen species: $f_A = n(A)/n$. Here

$$n = \rho(1 - y)/m_p = n(\text{H}) + n(\text{H}^+) + 2n(\text{H}_2). \quad (7)$$

(The abundance of H⁻ is much lower than the abundance of other hydrogen species and was neglected in the above equation.) Here ρ is the gas density, m_p is the mass of a proton, and y is the helium mass fraction. As the destruction of the ion H⁻ proceeds much more quickly than its production, the equilibrium fractional abundance of H⁻ can be estimated as

$$f_{\text{H}^-} = \frac{k_7 f_{\text{H}} f_{e^-}}{(k_8 + k_{15})f_{\text{H}} + (k_{16} + k_{17})f_{\text{H}^+} + k_{14}f_{e^-} + k_{23}/n}. \quad (8)$$

Furthermore, $f_{\text{H}^+} = f_{e^-}$ due to neutrality of helium and very low abundance of H⁻. In addition, the neutral hydrogen fractional

¹ See http://coho.mcmaster.ca/hydra/hydra_consort.html.

² See <http://cosmos.ucsd.edu/~tabel/PGas>.

abundance can be estimated from equation (7) as $f_{\text{H}} = 1 - f_{\text{H}^+} - 2f_{\text{H}_2}$. This leaves us with only two species whose fractional abundance has to be derived by solving differential equations: H^+ and H_2 . The corresponding equations are

$$\frac{1}{n} \frac{df_{\text{H}^+}}{dt} = k_1 f_e f_{\text{H}} - k_2 f_{\text{H}^+} f_e, \quad (9)$$

$$\frac{1}{n} \frac{df_{\text{H}_2}}{dt} = k_8 f_{\text{H}} f_{\text{H}} - f_{\text{H}_2} \left(k_{11} f_{\text{H}^+} + k_{12} f_e + k_{13} f_{\text{H}} + \frac{k_{27}}{n} \right). \quad (10)$$

2.2. Cooling

Molecular hydrogen molecules cool through radiative de-excitation of rovibrational levels. We adopted the H_2 cooling function from Galli & Palla (1998):

$$\Lambda_{\text{H}_2} = (\Lambda_{\text{LTE}}^{-1} + \Lambda_{n \rightarrow 0}^{-1})^{-1} n_{\text{H}_2} n_{\text{H}} \text{ ergs cm}^{-3} \text{ s}^{-1}, \quad (11)$$

where

$$\Lambda_{\text{LTE}} = \frac{1}{n} \left(\frac{9.5 \times 10^{-22} T_3^{3.76}}{1 + 0.12 T_3^{2.1}} e^{-(0.13/T_3)^3} + 3 \times 10^{-24} e^{-0.51/T_3} + 6.7 \times 10^{-19} e^{-5.86/T_3} + 1.6 \times 10^{-18} e^{-11.7/T_3} \right) \quad (12)$$

is the local thermodynamic equilibrium cooling function given by Hollenbach & McKee (1979, a sum of their eqs. [6.37] and [6.38]) and

$$\log \Lambda_{n \rightarrow 0} = -103.0 + 97.59 \log T - 48.05 (\log T)^2 + 10.80 (\log T)^3 - 0.9032 (\log T)^4 \quad (13)$$

is the density-independent low-density limit of the H_2 cooling function (Galli & Palla 1998). Here $T_3 \equiv T/10^3 \text{ K}$.

We also included five other cooling processes (the rates are taken from Anninos et al. 1997): atomic hydrogen line cooling,

$$\Lambda_{\text{HI}} = 7.50 \times 10^{-19} \left(1 + T_5^{1/2} \right)^{-1} e^{-118348/T} n_e n_{\text{H}}, \quad (14)$$

hydrogen collisional ionization cooling,

$$\Lambda_{\text{ion}} = 2.18 \times 10^{-11} k_1 n_e n_{\text{H}}, \quad (15)$$

hydrogen recombination cooling,

$$\Lambda_{\text{rec}} = 8.70 \times 10^{-27} T^{1/2} T_3^{-0.2} \left(1 + T_6^{0.7} \right)^{-1} n_e n_{\text{H}^+}, \quad (16)$$

bremsstrahlung cooling,

$$\Lambda_{\text{brem}} = 1.43 \times 10^{-27} T^{1/2} \left(1.1 + 0.34 e^{-(5.5 - \log T)^2/3} \right) n_e n_{\text{H}^+}, \quad (17)$$

and Compton cooling,

$$\Lambda_{\text{C}} = 1.017 \times 10^{-37} T_{\text{CMB}}^4 (T - T_{\text{CMB}}) n_e. \quad (18)$$

Here $T_5 \equiv T/10^5 \text{ K}$, $T_6 \equiv T/10^6 \text{ K}$, k_1 is the rate for reaction 1 (see Table 1), and $T_{\text{CMB}} = 2.73(1+z) \text{ K}$ is the temperature of the cosmic microwave background radiation, where z is the

redshift. The units for the cooling functions in equations (14)–(18) are $\text{ergs cm}^{-3} \text{ s}^{-1}$. The total cooling function is the sum of the cooling functions in equations (11) and (14)–(18).

2.3. Generating Initial Gas and DM Distributions

In our model we use periodic boundary conditions with the box size 5.7 times larger than the virial diameter of the DM halo. As the halo is located inside a relatively dense filament, we ignore the expansion of the universe. Both DM and baryons have zero global angular momentum.

The DM halo is assumed to have a Navarro-Frenk-White (NFW; Navarro et al. 1997) universal density profile,

$$\rho_{\text{DM}}(r) = \frac{\rho_{\text{DM},0}}{(r/r_s)(1+r/r_s)^2}, \quad (19)$$

where

$$\rho_{\text{DM},0} = \frac{m_{\text{vir}}}{4\pi r_s^3} \left[\ln(1+c) - \frac{c}{1+c} \right]^{-1}. \quad (20)$$

Here r_s is the scaling radius of the halo. In the Λ CDM cosmology, the typical concentration $c = r_{\text{vir}}/r_s$ of a DM halo with the virial mass $m_{\text{vir}} < 10^{11} M_{\odot}$ at the redshift z is

$$c = \frac{27}{1+z} \left(\frac{m_{\text{vir}}}{10^9 M_{\odot}} \right)^{-0.08} \quad (21)$$

(Bullock et al. 2001). Here r_{vir} is the virial radius of the halo. Zhao et al. (2003a, 2003b) showed that in cosmological N -body simulations c is always larger than ~ 3.5 .

Initially, the gas is isothermal with temperature $T_0 = 10^4 \text{ K}$, with fully ionized hydrogen and neutral helium, and is in hydrostatic equilibrium inside the periodic computational box containing one DM halo. Our choice for the initial temperature of the photoionized gas was guided by the results of the cosmological simulations of Ricotti et al. (2002) incorporating full radiative transfer and primordial chemistry. (In particular, from their Fig. 7 one can see that the temperature of the fully photoionized H II region surrounding a minigalaxy is very close to 10^4 K , despite the fact that the sources of ionizing radiation in this particular model are Population III stars that have a relatively hard spectrum.) The gas in our model has a primordial composition, with the helium mass fraction $y = 0.24$ and no metals. We produce this initial configuration in a two-step procedure as described next.

First, the computational box is filled homogeneously with N_g SPH gas particles with the temperature T_0 . We place a DM halo, represented by $N_{\text{DM}} = N_g$ particles, at the center of the box. The halo is truncated at a radius equal to the half-size of the box (5.7 times larger than the virial radius). The procedure outlined in Mashchenko & Sills (2005a) is used to generate the initial coordinates and velocity vectors of the DM particles (isotropy is assumed). Then we evolve the cube using Hydra for a very long time T_1 with the DM particles rigidly fixed in their original positions (static DM halo), the gas temperature fixed at T_0 (isothermal equation of state), and no chemical reactions. We fix the evolution time at $T_1 = 10 \text{ Gyr}$ for all our models, which is ~ 20 – 50 times longer than the sound crossing time in the box. At the end of the evolution, the gas density profile is well converged to its final hydrostatic shape down to the smallest resolved radius (containing 32 gas particles).

Second, we run the simulation for an additional 0.5–1 Gyr with the live DM halo (gas is still isothermal and fully ionized) to

TABLE 2
HALO PARAMETERS

z	$\log m_{\text{vir}}$ (M_{\odot})	c	r_s (kpc)	r_{vir} (kpc)	T_{vir} (K)	Box Size (kpc)	ε (pc)
20.....	7	3.50	0.0964	0.337	4890	3.81	6.6
15.....	6	3.50	0.0587	0.206	800	2.32	4.0
	6.5	3.50	0.0862	0.302	1730	3.41	5.9
	7	3.50	0.127	0.443	3720	5.00	8.7
	7.5	3.50	0.186	0.650	8020	7.34	13
10.....	7	3.55	0.182	0.644	2560	7.17	12

NOTES.—Here $T_{\text{vir}} = \mu V_{\text{vir}}^2/(2k)$ is the virial temperature of the halo, where $V_{\text{vir}}^2 = Gm_{\text{vir}}/r_{\text{vir}}$, k is the Boltzmann constant, and the mean particle mass is $\mu = 0.633m_p$ for primordial gas with fully ionized H and neutral He; ε is the gravitational softening length. All units are proper (not comoving).

allow the halo to (slightly) adjust itself to the presence of gas in the box. We stop the simulation before the central DM density profile starts getting flatter due to two-body interactions between DM particles.

One of the free parameters in our model is the average baryonic overdensity in the box, $\delta = \rho_0/\rho_b$, where ρ_0 is the average gas density in the box and

$$\rho_b = \frac{3H^2\Omega_b}{8\pi G}(1+z)^3 \quad (22)$$

is the average baryonic density in the universe. (Here G is the gravitational constant.) For the rest of this paper we assume a flat

universe with $\Omega_m = 0.27$, $\Omega_b = 0.044$, $H = 71 \text{ km s}^{-1} \text{ Mpc}^{-1}$, and $\sigma_8 = 0.84$ (Spergel et al. 2003). The parameter δ is meant to represent both the gas overdensity and the DM overdensity inside the box. Due to the small size of the box (~ 5 proper kpc), the DM that is not a part of the virialized DM halo is assumed to be distributed almost homogeneously and hence to have a negligible impact on the gas evolution inside the box. We do not include this DM in our simulations. In our models, when we vary the overdensity δ , we change only the average gas density, keeping the DM distribution unchanged.

Overall, we have four free parameters in our model: redshift z , DM halo virial mass m_{vir} , overdensity δ , and external radiation flux F_{21} . By running ~ 150 models, we explore a wide range in the initial parameters, with $z = 10\text{--}20$, $m_{\text{vir}} = 10^6\text{--}3 \times 10^7 M_{\odot}$, $\delta = 1\text{--}30$, and $F_{21} = 0\text{--}\infty$.

2.4. Numerical Simulations

We simulated six different DM halos (listed in Table 2). The main emphasis was on halos formed at $z = 15$ (four models), but we also considered one high-redshift ($z = 20$) and one low-redshift ($z = 10$) case for the fiducial virial mass of $10^7 M_{\odot}$. Each halo was simulated with four different values of overdensity δ : 1 (not inside a filament), 3 (low-density filament), 10 (filament), and 30 (partially collapsed halo). Each of the above 24 models was simulated with four to eight different values of the external Lyman-Werner flux F_{21} (including the case of zero flux), which resulted in ~ 120 models ran with full chemistry and cooling. The particular values of F_{21} (listed in Table 3) were chosen to bracket the

TABLE 3
RESULTS OF THE SIMULATIONS

z	$\log m_{\text{vir}}$ (M_{\odot})	δ	$\log F_{21}$ ($10^{-21} \text{ ergs s}^{-1} \text{ cm}^{-2} \text{ sr}^{-1} \text{ Hz}^{-1}$)	n_c (cm^{-3})	n_c/n_{out}	$\log F_{21,\text{crit}}$	t_{coll} (Myr)	$r_{\text{vir},1}$ (pc)	$m_{\text{vir},1}$ (M_{\odot})	$r_{\text{vir},2}$ (pc)	$m_{\text{vir},2}$ (M_{\odot})
20.....	7	1	$-\infty, -2, -1, 0, 0.5, 1, 2, \infty$	0.041	28	0.75	31	7	7.1×10^3	8	3.8×10^5
	7	3	$-\infty, -1, 0, 1, \infty$	0.13	30	∞	19	8	9.0×10^3	8	9.5×10^5
	7	10	$-\infty, -1, 0, 1, \infty$	0.52	37	∞	12	10	1.5×10^4	8	1.9×10^6
	7	30	$-\infty, 0, 1, 2, \infty$	4.2	110	∞	4	263	1.8×10^6	8	5.4×10^6
15.....	6	1	$-\infty, -3, -2, -1$	1.2×10^{-3}	1.6	$-\infty$	a
	6	3	$-\infty, -5, -4, -3.5, -3, -2, -1$	3.5×10^{-3}	1.6	-3.75	225	4	2.8×10^3	5	1.6×10^4
	6	10	$-\infty, -4, -3, -2.5, -2, -1, 0$	0.012	1.6	-2.75	102	5	3.7×10^3	5	2.6×10^5
	6	30	$-\infty, -2, -1.5, -1, 0$	0.035	1.6	-1.75	60	5	4.5×10^3	5	6.0×10^5
	6.5	1	$-\infty, -3, -2.5, -2, -1$	2.0×10^{-3}	2.7	-2.75	188	6	4.5×10^3	7	4.6×10^4
	6.5	3	$-\infty, -3, -2.5, -2, -1$	6.0×10^{-3}	2.8	-2.25	105	7	5.5×10^3	7	3.0×10^5
	6.5	10	$-\infty, -2, -1.5, -1, 0$	0.020	2.8	-1.25	56	7	7.0×10^3	7	7.9×10^5
	6.5	30	$-\infty, -2, -1, -0.5, 0$	0.063	2.9	-0.75	37	8	9.1×10^3	7	1.9×10^6
	7	1	$-\infty, -3, -2, -1.5, -1$	7.4×10^{-3}	11	-1.25	92	10	9.6×10^3	10	3.9×10^5
	7	3	$-\infty, -2, -1, -0.5, 0$	0.023	11	-0.25	47	10	1.1×10^4	10	9.9×10^5
	7	10	$-\infty, -1, 0, 1, \infty$	0.082	12	∞	28	13	1.6×10^4	10	2.5×10^6
	7	30	$-\infty, -1, 0, 1, \infty$	0.33	17	∞	18	18	3.1×10^4	10	6.3×10^6
	7.5	1	$-\infty, -1, 0, 1, \infty$	0.22	370	∞	18	17	2.4×10^4	15	1.2×10^6
	7.5	3	$-\infty, -1, 0, 1, \infty$	0.82	490	∞	11	27	5.8×10^4	15	3.0×10^6
7.5	10	b	
7.5	30	c	
10.....	7	1	$-\infty, -3, -2, -1$	1.1×10^{-3}	4.8	$-\infty$	447	12	1.1×10^4	14	3.2×10^4
	7	3	$-\infty, -3, -2.5, -2, -1$	3.3×10^{-3}	4.8	-2.25	201	13	1.3×10^4	15	7.6×10^5
	7	10	$-\infty, -2, -1.5, -1, 0$	0.011	5.0	-1.25	86	15	1.8×10^4	15	2.5×10^6
	7	30	$-\infty, -2, -1, 0, 0.5, 1, 2, \infty$	0.038	5.6	0.5	52	19	2.8×10^4	15	5.8×10^6

NOTES.—Here $\log F_{21} = -\infty$ corresponds to no external radiation, $\log F_{21} = \infty$ stands for no H₂ cooling, n_c and n_{out} are the initial gas density at the center of the halo and at the edge of the computational box, respectively, and $F_{21,\text{crit}}$ is the critical value for F_{21} (such that models with $F_{21} \gtrsim F_{21,\text{crit}}$ will not collapse in one local Hubble time). Parameters t_{coll} , $r_{\text{vir},1}$, $m_{\text{vir},1}$, $r_{\text{vir},2}$, and $m_{\text{vir},2}$ correspond to models with $F_{21} = 0$. Here t_{coll} is the time when the Jeans criterion is met inside the halo, $r_{\text{vir},1}$ and $m_{\text{vir},1}$ are the radius and the enclosed gas mass of the region with the smallest virial ratio at $t = t_{\text{coll}}$, and $r_{\text{vir},2}$ and $m_{\text{vir},2}$ are the same quantities at the end of simulations.

a The model does not collapse even when $F_{21} = 0$.

b The model collapsed during the evolution of isothermal gas in a live DM halo (the second step in generating the hydrostatic initial conditions).

c The model collapsed during the evolution of isothermal gas in the static DM halo potential (the first step in generating the hydrostatic initial conditions).

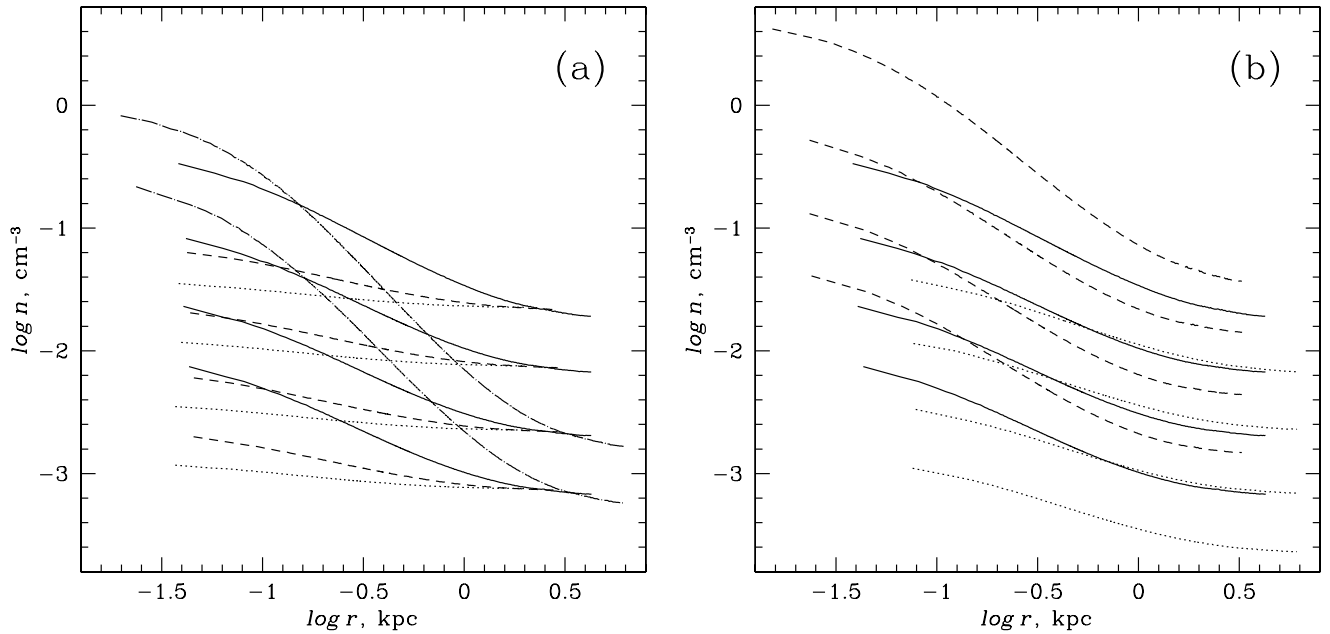


FIG. 1.—Initial hydrostatic radial gas density profiles for all our models. Models with larger δ are located higher. (a) Halos at fixed redshift $z = 15$. Dotted, dashed, solid, and dot-dashed lines correspond to the models with $\log m_{\text{vir}} = 6, 6.5, 7, \text{ and } 7.5$, respectively. For the case of $\log m_{\text{vir}} = 7.5$, only the models with $\delta = 1$ and 3 are shown. (b) Halos with fixed virial mass $m_{\text{vir}} = 10^7 M_{\odot}$. Dotted, solid, and dashed lines correspond to the models with $z = 10, 15, \text{ and } 20$, respectively.

minimum value of the flux $F_{21,\text{crit}}$ when the external radiation prevents the halo from collapsing.

The virial temperature of our halos is below the initial gas temperature of 10^4 K for the case of fully ionized hydrogen and would be above 10^4 K, if the gas were neutral, only for our most massive halo with $m_{\text{vir}} \simeq 3 \times 10^7 M_{\odot}$ (see Table 2). The gravitational softening length ε was set to be commensurable with the average interparticle distance within the virial extent of the DM halo: $\varepsilon = 1.8r_h/N_{\text{DM}}^{1/3}$. (Here r_h is the half-mass radius of the halo.) All of the above models had a total number of particles of $2 \times 64^3 \simeq 520,000$.

As one can see from Table 2, the concentration of our halos is close to 3.5 due to the constraint of Zhao et al. (2003a, 2003b). The virial radius of these objects is very small: between 200 and 650 pc. The size of the periodic computational box is between 2.3 and 7.3 proper kpc.

The central hydrogen number density n_c in the initial hydrostatic state spans a wide range: $0.001\text{--}4 \text{ cm}^{-3}$ (Table 3). This excludes the two most massive models ($\log m_{\text{vir}} = 7.5$) with the largest overdensities, $\delta = 10$ and 30 , which collapsed during the generation of the initial gas and DM distributions (see § 2.3). As one can see from Table 3, the gas density contrast n_c/n_{out} between the center of the halo and the edge of the box initially ranges from 1.6 (i.e., the gas is barely perturbed by the shallow gravitational potential of the DM halo) for our lowest mass halo with $m_{\text{vir}} = 10^6 M_{\odot}$ to ~ 500 for the model with $m_{\text{vir}} \simeq 3 \times 10^7 M_{\odot}$ and $\delta = 3$. For models with larger m_{vir} , δ , and/or z the ratio n_c/n_{out} increases noticeably with δ , indicating that the gas self-gravity becomes important for such models (Table 3). Figure 1 plots the initial density profiles for all our models.

We consider a halo to have collapsed if within time t_{H} , comparable to the local Hubble time, the gas becomes Jeans unstable within the virial extent of the DM halo. For our models with $z = 20, 15, \text{ and } 10$ we set $t_{\text{H}} = 200, 300, \text{ and } 500$ Myr, respectively. We define gas to be Jeans unstable if for some radius $r < r_{\text{vir}}$ the virial ratio

$$\nu = -2K(r)/W(r) \quad (23)$$

becomes less than unity. Here $K(r)$ and $W(r)$ are the thermal and potential energy, respectively, for the enclosed gas. We derive $W(r)$ from the kernel-smoothed SPH gas density ϱ :

$$W(r) = -4\pi G \int_0^r \varrho M(r) r dr \quad (24)$$

(Binney & Tremaine 1987, p. 68). For consistency, the enclosed gas mass $M(r)$ in the above equation is also derived from the smoothed gas density ϱ : $M(r) = 4\pi \int \varrho r^2 dr$. In equation (24) we ignore the potential energy of the DM halo as it becomes significantly smaller than the potential energy of the gas at advanced stages of the gas collapse. Using the smoothed gas density ϱ results in $W(r)$ being still smaller. As a consequence, our Jeans collapse criterion is a conservative one, as in a real system the potential energy for the enclosed gas would be larger, resulting in smaller virial ratio ν .

3. RESULTS OF SIMULATIONS

When the flux of the external Lyman-Werner radiation is equal to zero, virtually all of our models collapse within one local Hubble time. The only exception is the least massive model with $m_{\text{vir}} = 10^6 M_{\odot}$ ($T_{\text{vir}} = 800$ K) and $\delta = 1$. For the rest of the models, the collapse time t_{coll} ranges from $0.02t_{\text{H}}$ to $\sim 0.9t_{\text{H}}$ (see Table 3). The radius of the region becoming Jeans unstable, r_{vir} , is always slightly larger than the softening length ε , indicating that the collapse is severely underresolved in our simulations. We address the issue of numerical convergence at the end of this section. The mass of the unstable gas is between 3×10^3 and $6 \times 10^4 M_{\odot}$ initially but becomes much larger (more than $10^6 M_{\odot}$ in many cases) by the end of the simulations due to ongoing accretion of the gas on the central core. In many collapsed models we could not continue simulations until the very end as these runs were virtually brought to a stop due to the extremely large gas densities developed at the center of the halo. As a result, the $m_{\text{vir},2}$ values we list in Table 3 should be considered as a lower limit. The precise value is probably not very important, as in real systems

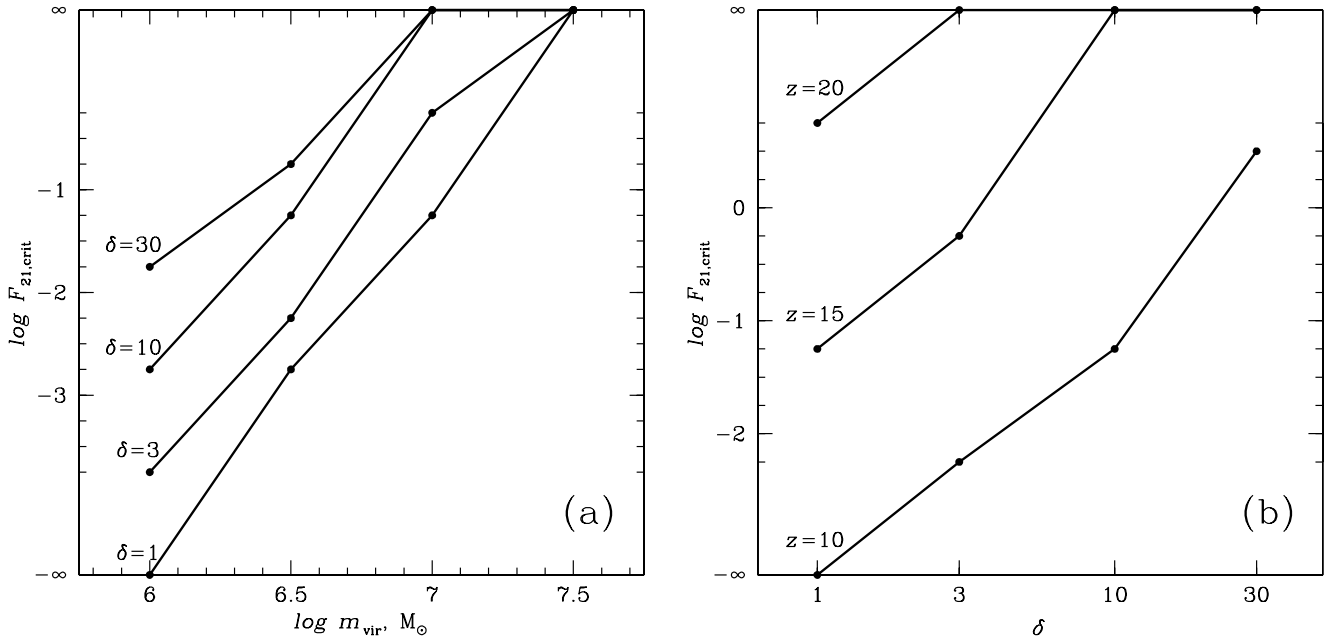


FIG. 2.—Critical Lyman-Werner flux $F_{21,crit}$ for our models. Areas above the lines correspond to halos that do not collapse within one local Hubble time, and below the lines to those that do collapse. (a) Halos at fixed redshift $z = 15$. (b) Halos with fixed virial mass $m_{vir} = 10^7 M_\odot$.

a starburst should occur some time after the core becomes Jeans unstable, which would dramatically change the following evolution of the minigalaxy.

The main results of our work are summarized in Figure 2 and Table 3. In Figure 2 we plot the critical value of the Lyman-Werner flux $F_{21,crit}$ for all our models as a function of m_{vir} , δ , and z . Models with $F_{21} < F_{21,crit}$ collapse within a local Hubble time and do not collapse for larger fluxes. From Figure 2 one can see that the impact of external photodissociating radiation is most significant for halos with $m_{vir} \lesssim 3 \times 10^6 M_\odot$ and $\delta \lesssim 10$, where even a small flux $F_{21} \sim 0.01$ can prevent the halo from collapsing at a redshift of 15. As Figure 2b shows, $F_{21,crit}$ is a very strong function of z . At $z = 20$, the halo with $m_{vir} = 10^7 M_\odot$ will collapse even outside a cosmological filament ($\delta = 1$), whereas at $z = 10$ the halo with $m_{vir} = 10^7 M_\odot$ can collapse only for $\delta \gtrsim 20$ (if $F_{21} \sim 1$). Halos with a given virial mass are more immune to the external Lyman-Werner radiation at larger z due to a combination of several factors: (1) halos with the same m_{vir} have larger virial temperature at larger z (see Table 2), (2) the average gas density in the universe grows as $\sim z^3$ (eq. [22]), and (3) the temperature of the cosmic microwave background grows as $z + 1$, resulting in much stronger Compton cooling at larger redshifts (see eq. [18]).

On a more detailed level, the impact of varying the Lyman-Werner flux on gas dynamics can be seen in Figure 3. Here we plot the central gas density and temperature as a function of time for our fiducial halo with $m_{vir} = 10^7 M_\odot$, $z = 15$, and $\delta = 3$ for different values of F_{21} . From this plot one can see that a larger photodissociation flux results in the central gas density growing more slowly and the central gas temperature decreasing more slowly. Also, the final temperature of the collapsed core increases with increasing flux, reaching ~ 800 K for $\log F_{21} = -0.5$. It takes longer for the core to become Jeans unstable (Fig. 3, circles) for larger F_{21} . When the flux reaches $\log F_{21} = 0$, no collapse occurs within the evolution time of 300 Myr, although the central temperature decreases to ~ 2000 K and the central density grows to $\sim 30 \text{ cm}^{-3}$.

Figure 4 can be used to estimate the importance of different physical processes on the dynamics of the collapsing halo. Here

we show the evolution of the lowest value of the virial ratio ν within the virial extent of the halo for our fiducial case with $m_{vir} = 10^7 M_\odot$, $z = 15$, $\delta = 3$, and $F_{21} = 0.1$. We show the results for a full run (solid line) and for a few additional simulations with some of the physical processes turned off. The first most obvious effect is that turning the H_2 cooling off changes the dynamics dramatically: when the H_2 cooling is included, the core collapses after ~ 140 Myr, whereas when $\Lambda_{\text{H}_2} = 0$, the halo is very far from a collapse even at the end of the simulations (after 300 Myr). Another interesting result is that the impact of the photodetachment of H^- (reaction 23 in Table 1; eq. [4]) on the overall collapse dynamics is negligible, despite the fact that we use the

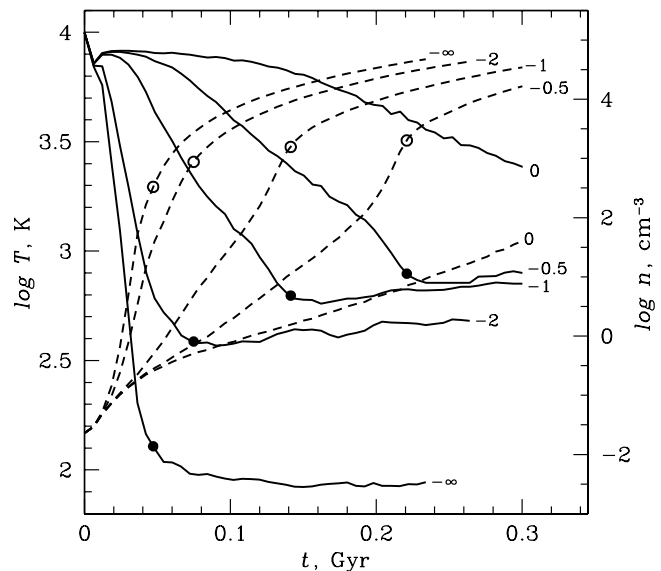


FIG. 3.—Evolution of the gas properties at the center of the halo with $m_{vir} = 10^7 M_\odot$, $z = 15$, $\delta = 3$, and $\log F_{21} = -\infty, -2, -1, -0.5$, and 0 . We show the gas temperature T (solid lines) and density n (dashed lines). Numbers next to the lines mark the values of $\log F_{21}$. Filled circles (for solid lines) and open circles (for dashed lines) mark the time when the halo core becomes Jeans unstable.

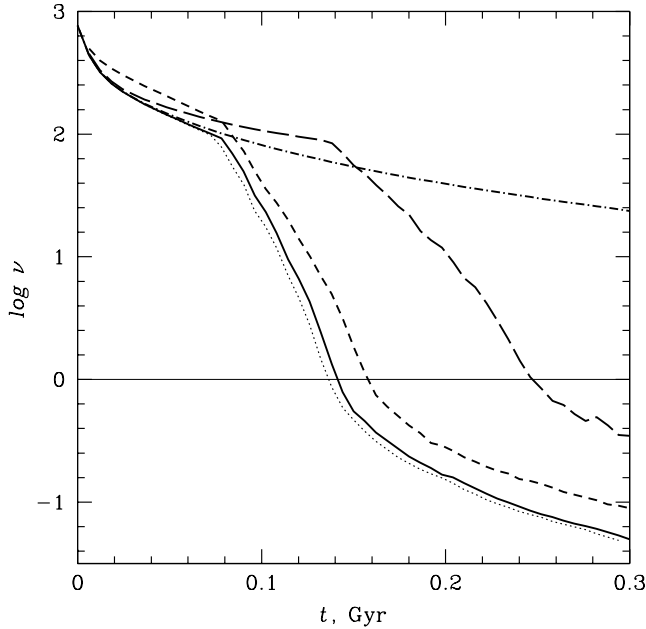


FIG. 4.—Evolution of the lowest value of the virial ratio ν for a halo with $m_{\text{vir}} = 10^7 M_{\odot}$, $z = 15$, $\delta = 3$, and $F_{21} = 0.1$. *Solid line*: Full chemistry. *Dotted line*: Model with no photodetachment of H^- ($k_{23} = 0$). *Short-dashed line*: Model with $\Lambda_{\text{C}} = 0$ (the case with $\Lambda_{\text{rec}} = 0$ is virtually identical). *Long-dashed line*: Model with $\Lambda_{\text{H1}} = 0$. *Dot-dashed line*: Model with negligible H_2 cooling ($F_{21} = 1$).

most conservative power-law exponent $\alpha = -1$ to describe the spectrum of the external radiation (corresponding to radiation produced by quasars). In a more realistic case, at least a fraction of the external radiation flux should come from stellar sources, further reducing the importance of the H^- photodetachment reaction on dynamics of minigalaxies in defunct cosmological H II regions. It follows that the only important photoreaction for our objects is the direct photodissociation of H_2 molecules by Lyman-Werner photons.

From the analysis of Figure 4 it appears that the next most significant process (after H_2 cooling) is the atomic hydrogen line cooling (*long-dashed lines*), followed by Compton cooling and hydrogen recombination cooling. The rest of the cooling processes have negligible impact on the evolution of the halo. We draw the reader's attention to the fact that the importance of the H line cooling is a strong function of the assumed initial temperature of the fully photoionized gas. For example, lowering T_0 from 10^4 to 8×10^3 K reduces the initial values of Λ_{H1} by a factor of ~ 20 (see eq. [14]). It also lowers the ratio T_0/T_{vir} , so the overall dynamics of the collapse should not be affected much. We conclude that at the redshift of ~ 15 atomic hydrogen line cooling, Compton cooling, and hydrogen recombination cooling are of roughly comparable importance for the dynamics of our minigalaxies.

In Figure 5 we plot the radial profiles for our fiducial halo for three different times $t \simeq 6, 144$ (when the core becomes Jeans unstable), and 300 Myr. As one can see in Figure 5a, initially the core becomes unstable at the very center of the halo, later involving the whole virial extent of the halo. Figure 5b demonstrates that at the late stages of the collapse a dominant fraction of the total gas mass inside the virial radius of the halo has been accreted by the core and that the accretion proceeds with increasingly larger gas radial infall speeds. A very interesting effect can be seen in Figures 5c and 5d: after the core becomes Jeans unstable, the infalling gas becomes increasingly hotter near the core due to adiabatic compression, leading to an increasingly larger hydrogen ionization fraction near the core and, as a result, to increased H_2

production in this area. This, in turn, increases cooling of the gas in the central parts of the halo, accelerating the overall collapse process. It thus appears that gas in minigalaxies forming in the defunct cosmological H II regions can be effectively cooled by H_2 molecules formed due to high nonequilibrium abundance of free electrons not only initially, before the onset of the collapse, but also at the advanced stages of the collapse. This leads to a much more significant positive feedback of ionizing radiation on star formation in small galaxies in the early universe.

From the analysis of Figure 5 it is obvious that the collapse is severely underresolved in our models. For example, one can see the gas infall velocity discontinuity around a radius of $\sim 1.3\epsilon$ (Fig. 5b) and dramatic changes in temperature and density slopes at the same radius (Fig. 5c). The important question is then, how robust are our above conclusions given that the collapse is not fully resolved?

Unfortunately, it is not feasible to run higher resolution simulations with our scalar version of the code Hydra. Instead, we address the above issue by rerunning our models with $m_{\text{vir}} = 10^7 M_{\odot}$ and $z = 15$ with two different numbers of particles, $2 \times 32^3 \simeq 66,000$ and $2 \times 64^3 \simeq 520,000$, with the size of the periodic computational box being twice smaller than in the original simulations: 2.5 instead of 5 kpc. In half-box simulations the initial hydrostatic gas distribution and overall collapse dynamics are somewhat different from the full-box simulations, so these new runs are not meant to be directly compared with the original simulations. Instead, one has to compare the half-box low-resolution simulations (which have the same spatial resolution as our original runs: $\epsilon = 8.7$ pc) with the half-box high-resolution simulations (spatial resolution is twice better: $\epsilon = 4.3$ pc).

The details of the half-box simulations are provided in Table 4 (analog of Table 3). One can see from this table that in the higher resolution simulations the collapse takes place $\sim 25\%$ earlier at a twice smaller radius and involves initially 2–3 times less gas. The dynamics of the collapse for both cases can be followed in Figure 6, where we show the evolution of the central gas density and temperature for our fiducial halo. As one can see in Figure 6, the central gas density grows faster and reaches larger values in the higher resolution simulations. Importantly, in the higher N case the growth rate of the gas density is not affected by spatial resolution even for some time after the onset of the Jeans instability (Fig. 6, *open circles*), whereas in the lower resolution case the sharp change in the density growth rate takes place at the onset of the instability. This indicates that at least the initial stage of the core collapse is resolved in our higher resolution simulations. Interestingly, the final central temperature of the gas is the same in both cases (see Fig. 6).

It is easy to see why in the higher resolution case the collapse takes place earlier. Indeed, from Figure 1 one can see that all our initial hydrostatic gas density profiles have a cusp with a small slope at the center of the halo. As a result, the higher the spatial resolution of the simulations, the larger is the initial density of the resolved gas in the core, leading to stronger cooling and faster evolution. As the slope of the density cusp is small, we expect this process to converge at some large N . Indeed, as we progress to larger N , a very moderate increase in the resolved gas density (and hence of the cooling rate) would correspond to much smaller mass of the gas affected by the cooling, resulting in negligible impact on the dynamics of the system for large enough N . More quantitatively, if the initial gas density near the halo center is $\propto r^{-\alpha}$ and the spatial resolution is ϵ , then the mass of the unresolved core is $M_c \propto \epsilon^{3-\alpha}/(3-\alpha)$ and the average core density is $\rho_c \propto \epsilon^{-\alpha}/(3-\alpha)$. As the cooling per atom is proportional to ρ_c , the global core cooling is proportional to $M_c \rho_c \propto \epsilon^{3-2\alpha}/(3-\alpha)^2$, which

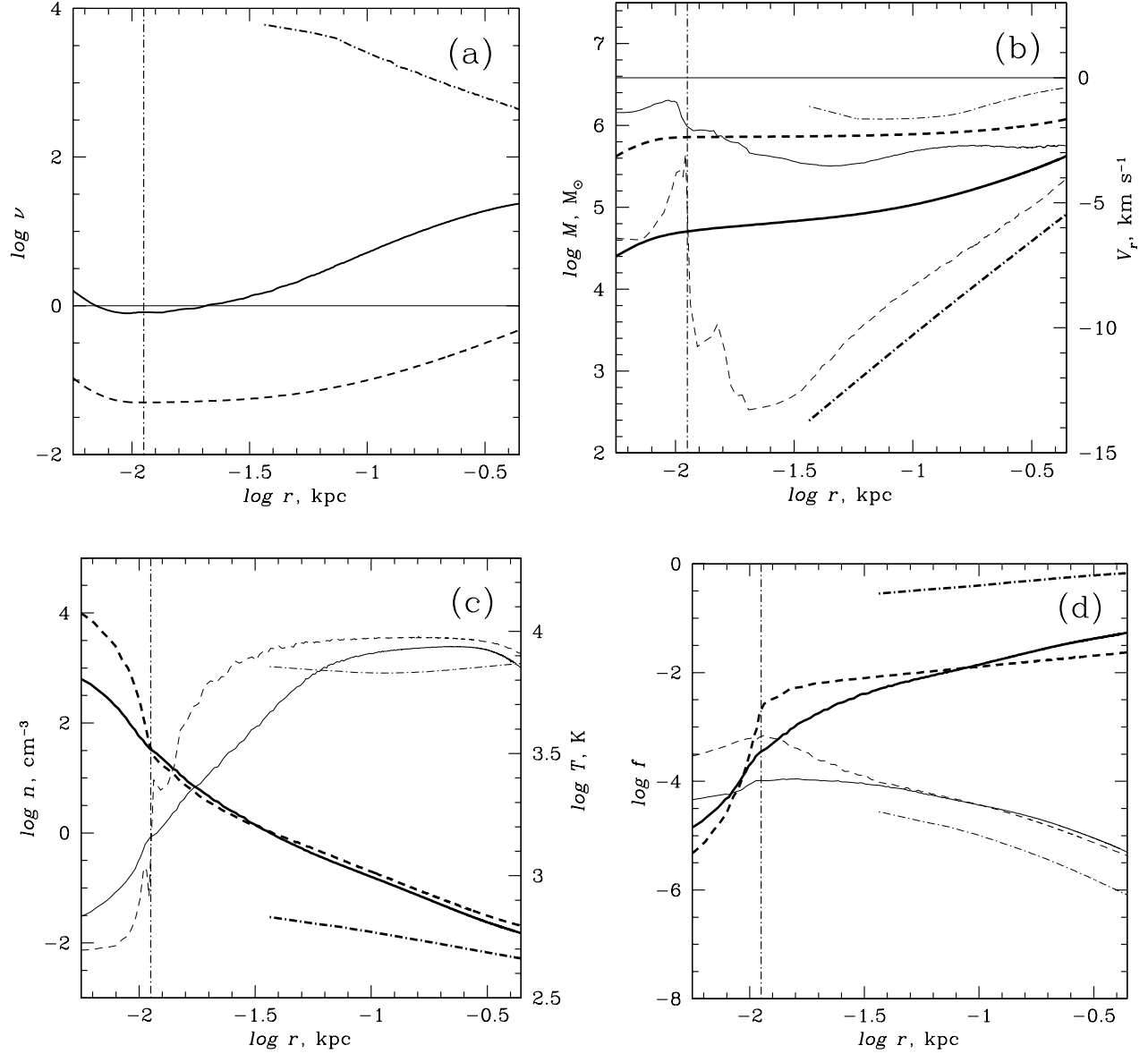


FIG. 5.—Radial profiles for a halo with $m_{\text{vir}} = 10^7 M_{\odot}$, $z = 15$, $\delta = 3$, and $\log F_{21} = -1$ at three different times: at the early epoch ($t = 6$ Myr; dot-dashed lines), around the time when the gas became Jeans unstable ($t = 144$ Myr; solid lines), and at the end of the simulations ($t = 300$ Myr; dashed lines). Vertical dot-dashed lines correspond to the spatial resolution 1.3ϵ . (a) Virial ratio ν . Parts of the lines below the horizontal line $\log \nu = 0$ are Jeans unstable. (b) Mass M of the gas enclosed within radius r (thick lines) and radial gas velocity V_r (thin lines). The horizontal solid line corresponds to $V_r = 0$. (c) Gas density n (thick lines) and temperature T (thin lines). (d) Fractional abundances f_{H^+} (thick lines) and f_{H_2} (thin lines).

TABLE 4
HALF-BOX SIMULATIONS FOR A HALO WITH $\log m_{\text{vir}} = 7$ AND $z = 15$

N	δ	$\log F_{21}$ (10^{-21} ergs s^{-1} cm^{-2} sr^{-1} Hz^{-1})	n_c (cm^{-3})	n_c/n_{out}	$\log F_{21,\text{crit}}$	t_{coll} (Myr)	$r_{\text{vir},1}$ (pc)	$m_{\text{vir},1}$ (M_{\odot})	$r_{\text{vir},2}$ (pc)	$m_{\text{vir},2}$ (M_{\odot})
2×32^3	1	$-\infty, -3, -2, -1.5, -1$	5.8×10^{-3}	6.9	-1.25	103	10	9.0E+03	10	2.4E+05
	3	$-\infty, -2, -1, -0.5, 0$	0.018	6.9	-0.75	51	11	1.0E+04	10	7.5E+05
	10	$-\infty, -1, 0, 0.5, 1, \infty$	0.062	7.2	0.25	31	11	1.2E+04	10	2.4E+06
	30	$-\infty, -1, 0, 1, \infty$	0.22	8.0	∞	21	26	5.0E+04	10	6.1E+06
2×64^3	1	$-\infty, -3, -2, -1.5, -1$	7.8×10^{-3}	9.2	-1.25	85	5	4.4E+03	5	5.7E+04
	3	$-\infty, -2, -1, -0.5, 0$	0.024	9.2	-0.75	40	5	4.9E+03	5	1.4E+05
	10	$-\infty, -1, 0, 0.5, 1, \infty$	0.083	9.6	0.25	22	6	6.3E+03	5	3.4E+05
	30	$-\infty, -1, 0, 1, \infty$	0.30	11	∞	15	9	1.4E+04	5	9.0E+05

NOTES.—Here N is the total number of particles (DM+gas). The rest of the notations are the same as in Table 3.

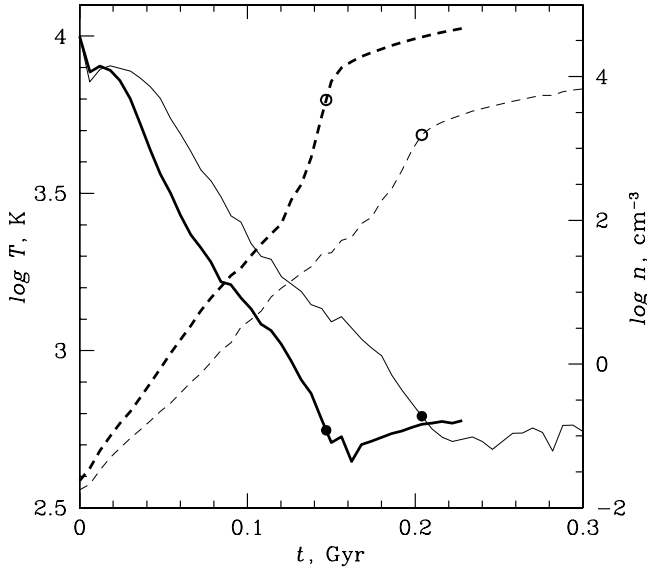


FIG. 6.—Evolution of the gas temperature (*solid lines*) and density (*dashed lines*) at the center of the halo with $m_{\text{vir}} = 10^7 M_{\odot}$, $z = 15$, $\delta = 3$, and $\log F_{21} = -1$ in half-box simulations. Thick and thin lines correspond to high- ($N = 2 \times 64^3$) and low-resolution ($N = 2 \times 32^3$) simulations. Filled (for solid lines) and open (for dashed lines) circles mark the time when the halo core becomes Jeans unstable.

approaches zero as $\varepsilon \rightarrow 0$ ($N \rightarrow \infty$) for shallow cusps with $\alpha < 1.5$. All of our models initially had $\alpha = 0.11$ – 0.55 .

Figure 7 allows a detailed comparison of the final gas profiles in our half-box simulations for the cases of low and high resolution. From Figure 7*b* one can see that the final mass of the collapsed gas is comparable in the both cases and that the gas infall velocity discontinuity is even sharper and takes place at a twice smaller radius in the higher N case. Most importantly, the higher resolution simulations confirm and reinforce our above conclusion that the nonequilibrium formation of H_2 molecules in our objects is not restricted to the initial stage of the collapse and is instead an ongoing process, becoming potentially even more important at the advanced stages of the collapse. This is evident in Figures 7*c* and 7*d*, which show that in the higher resolution simulations the gas temperature near the core is even higher, with the hot gas zone extending to even smaller radius, than in the lower N case, resulting in higher nonequilibrium electron abundance and hence higher H_2 abundance in the core region.

It is not clear from the above results if our higher resolution half-box simulations are close to numerical convergence. Nevertheless, by comparing our low- and high- N simulations, we can make a robust conclusion that the models presented in this paper capture the essence of the gas collapse process in primordial minigalaxies forming in defunct cosmological H II regions. Our results are conservative in the sense that higher resolution, and presumably more realistic, simulations would lead to minigalaxies forming even faster and potentially even under larger fluxes of external Lyman-Werner radiation.

4. DISCUSSION AND CONCLUSIONS

The traditional point of view is that soon after the formation of the first stars in the universe inside small halos at $z > 20$ the formation of the next generation of minigalaxies with $T_{\text{vir}} < 10^4$ K was suppressed due to buildup of the metagalactic H_2 photodissociating background (Haiman et al. 2000). Recent cosmological (Ricotti et al. 2002) and semic cosmological (O’Shea et al. 2005) simulations with radiative transfer questioned the above argument

by showing that in defunct cosmological H II regions in overdense regions of the early universe ($z > 10$) the formation of the minigalaxies can be boosted due to nonequilibrium chemistry. In our paper we study the above mechanism of positive feedback of ionizing radiation on small galaxy formation by running a large set of simulations of galaxy formation inside defunct H II regions. By employing a noncosmological approach, we produced a sequence of models with precisely controlled and reproducible (although idealized) initial and boundary conditions. This helped us to focus on the most relevant physical processes at work in our objects.

Most importantly, we derived the critical fluxes of the background Lyman-Werner radiation sufficient to prevent the collapse of gas in minigalaxies with $T_{\text{vir}} < 10^4$ K at $z = 10$ – 20 . We showed that the positive feedback mechanism becomes much more efficient at larger z for galaxies with given virial mass and confirmed the result of Ricotti et al. (2002) that it is efficient inside filaments with the overdensity of $\gtrsim 10$. We studied the details of the process of the gas collapse in a preionized minigalaxy exposed to external Lyman-Werner radiation. We conclude that, similarly to the canonical case of small galaxy formation in non-ionized regions of the universe (Machacek et al. 2001), the reaction of photodetachment of H^- has a negligible impact on the dynamics of the collapse. This leaves the direct photodissociation of H_2 molecules by metagalactic Lyman-Werner radiation as the only important photoreaction. We identified the H_2 , hydrogen line, Compton, and hydrogen recombination coolings as the only important cooling processes. Hydrogen collisional ionization cooling and bremsstrahlung cooling are shown to be not important for our objects.

We found that for the minigalaxies forming in defunct H II regions the nonequilibrium H_2 formation has an important dynamical effect not only during the initial phase, leading to the core of the galaxy becoming Jeans unstable, but also later on during the advanced stages of the core collapse. This mechanism allows the core of the minigalaxy to accrete significant mass by the time the central starburst disrupts the accretion.

Our results give further support to the Ricotti et al. (2002) picture of formation and evolution of minigalaxies in the early universe. In this picture, first minigalaxies form at high redshift ($z > 20$), when the metagalactic Lyman-Werner background is close to zero, due to cosmological nonzero residual fraction of free electrons resulting in efficient H_2 cooling. The stars in the minigalaxy ionize gas inside the halo and in nearby halos, creating conditions for efficient H_2 cooling due to nonequilibrium electron abundance after the Population III stars (believed to be very massive and short lived) die. As we confirmed here, this process is tolerant to relatively large fluxes of the external Lyman-Werner radiation. The process can repeat itself with a timescale of a few tens of millions of years (Ricotti et al. 2002; O’Shea et al. 2005; this paper), allowing the minigalaxy to survive through the “difficult times” of the universe being filled with the H_2 photodissociating radiation until the universe is reionized before $z \sim 7$. These repetitive local starbursts will result in the metallicity of the local intergalactic medium increasing with time. If the metallicity becomes larger than $\sim 10^{-3} Z_{\odot}$, the star formation will switch from Population III to Population II mode (e.g., Bromm et al. 2001), producing a long-living stellar population, which should survive until the present time. The size of the collapsed cores in our simulations is very small ($\lesssim 5$ pc) and is comparable to the sizes of globular clusters. It is tempting then to associate this final Population II starburst at the core of the minigalaxy with the formation of a metal-poor globular cluster, at least for the halos with the lowest values of the specific angular momentum.

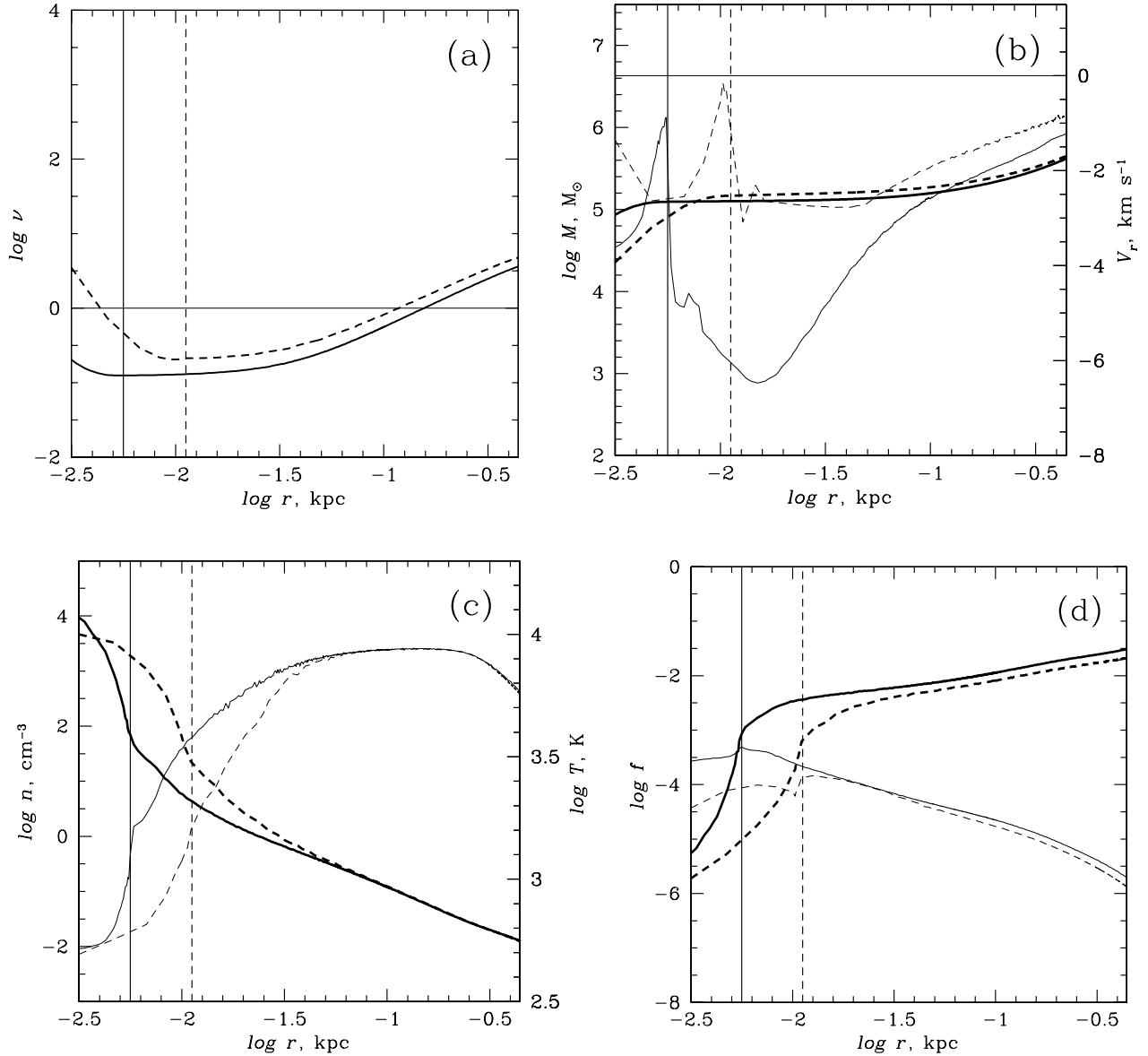


FIG. 7.—Final radial profiles for a halo with $m_{\text{vir}} = 10^7 M_{\odot}$, $z = 15$, $\delta = 3$, and $\log F_{21} = -1$ for half-box simulations at two different resolutions: $N = 2 \times 64^3$ (solid lines) and $N = 2 \times 32^3$ (dashed lines). Vertical lines mark the corresponding spatial resolutions, 1.3ϵ . (a) Virial ratio ν . Parts of the lines below the horizontal line $\log \nu = 0$ are Jeans unstable. (b) Enclosed gas mass M (thick lines) and radial gas velocity V_r (thin lines). The horizontal solid line corresponds to $V_r = 0$. (c) Gas density n (thick lines) and temperature T (thin lines). (d) Fractional abundances f_{H^+} (thick lines) and f_{H_2} (thin lines).

We showed (Mashchenko & Sills 2005b) that the DM halos of such objects can be tidally stripped when they are accreted by larger galaxies. This could be considered as a revised version of the primordial picture of globular cluster formation of Peebles & Dicke (1968) and Peebles (1984). Alternatively, these surviving minigalaxies could end up contributing to the population of dwarf spheroidal galaxies (Ricotti & Gnedin 2005).

In § 3 we discussed the impact of the limited resolution on the results of our simulations. Our conclusion was that even though our highest spatial resolution simulations could not completely resolve the dynamics of the collapsing core, we believe that we captured the essence of the collapse process. We want to emphasize that in our simulations the physics driving the collapse (primordial chemistry and cooling) is resolved much better than hydrodynamics. As Figure 5d demonstrates, during the most critical initial phase of the core collapse the enhanced nonequilibrium production of H_2 molecules is not restricted to the core region and instead takes place over a wide range of distances from the

center of the halo. Another confirmation of the chemistry being well resolved in our models can be found in Table 4, where one can see that the critical fluxes of the external photodissociating radiation $F_{21,\text{crit}}$ are the same for both lower and higher resolution (half-box) simulations.

Recently, Glover et al. (2005) used the results of their simulations of the collapse of gas in a photoionized small galaxy in the early universe to argue that the uncertainties in the rate coefficients for reactions 8 and 16 (see Table 1) can lead to an order-of-magnitude uncertainty in the value of the critical flux of the external photodissociating radiation. We cannot comment on this as we have not explored in our models the consequences of the uncertainties in the rates for the above reactions being large. If the results of Glover et al. (2005) are confirmed, this would potentially lead to up to a factor of a few error in our values of $F_{21,\text{crit}}$, with all the values being either systematically larger or smaller. We want to emphasize that it would not change our qualitative result that the efficient formation of minigalaxies in fossil

cosmological H II regions is possible even under relatively large levels of the metagalactic Lyman-Werner radiation.

How are our results affected by the simplifying assumptions we have made? One of our model assumptions is that the process of photoevaporation of the minigalaxy is complete, with the gas becoming 100% ionized and reaching the state of hydrostatic equilibrium in the halo gravitational potential. This assumption allowed us to significantly reduce the uncertainty in the initial conditions. In reality, in many (perhaps most) cases, the gas in our objects would only be partially photoionized. The reason for this is that the typical sources of ionizing radiation at this early epoch would be massive stars (individual or in small clusters), with their lifetimes being too short to allow the gas in the galaxy, which is being photoevaporated, to reach a state of hydrostatic equilibrium. Assuming that initially the gas was almost neutral and had a temperature commensurate with the virial temperature of the halo $T_{\text{vir}} < 10^4$ K, an incomplete photoevaporation would result in a partially ionized gas with the core density larger than in the fully photoionized state. It is reasonable to assume that such a system should collapse at least as easily (or even easier) as a fully photoionized one, as long as the electron abundance of the photoionized gas is significantly larger than the residual cosmological value of $\sim 2 \times 10^{-4}$. In this sense, the above assumption is a conservative one.

Our assumption of the gas being optically thin to radiation is also a conservative one, as the self-shielding of the gas would reduce the Lyman-Werner radiation flux near the center of the halo, where the production of H₂ molecules takes place during the advanced stages of the core collapse. In our fiducial halo simulated with the highest spatial resolution (half-box simulations with $N = 2 \times 64^3$), the optical depth for Lyman-Werner photons traveling from the outside of the halo to the smallest resolved radius of ~ 5 pc is around unity, indicating that self-shielding can be important for our objects (especially at the late stages of the core collapse).

Nagakura & Omukai (2005) used one-dimensional hydrodynamic simulations incorporating nonequilibrium primordial gas chemistry to show that the gas cooling due to HD molecules can be an important dynamical factor at the late stages of the gas collapse in previously photoionized minigalaxies. Recently, Lipovka et al. (2005) published a revised HD cooling function, with the cooling efficiency being larger than previously reported (especially for hot and dense gas). This could potentially make the HD molecule cooling even more important for the dynamics of the collapsing gas in small primordial galaxies. We did not include HD chemistry in our model as these reactions would only become important when the collapsing core is no longer well resolved in our simulations. If included, the additional cooling due to HD molecules would only strengthen our conclusions.

If gas in photoevaporated minigalaxies has significant global angular momentum, this could affect our results and conclusions. The effect of angular momentum will be strongest during the advanced stages of the gas collapse. Instead of a spherical core, a central disk will be formed, reducing the central gas density. We argue that the nonzero angular momentum should not qualitatively change our main conclusions, as the nonequilibrium H₂ formation, leading to the gas in the minigalaxy becoming Jeans unstable, takes place over a wide range of radial distances (see the thin solid line in Fig. 5*d*), not just in the central densest region. Machacek et al. (2001) noted that the ability of a cloud to collapse does not seem to strongly depend on the angular momentum of its DM halo. In any event, our results should be directly applicable to minigalaxies with low values of the global gas angular momentum.

The simulations reported in this paper were carried out on the McKenzie cluster at the Canadian Institute for Theoretical Astrophysics. H. M. P. C. acknowledges support from the Canadian Institute for Advanced Research and NSERC.

REFERENCES

- Abel, T., Anninos, P., Norman, M. L., & Zhang, Y. 1998, *ApJ*, 508, 518
 Abel, T., Anninos, P., Zhang, Y., & Norman, M. L. 1997, *NewA*, 2, 181
 Abel, T., Bryan, G. L., & Norman, M. L. 2002, *Science*, 295, 93
 Anninos, P., Zhang, Y., Abel, T., & Norman, M. L. 1997, *NewA*, 2, 209
 Binney, J., & Tremaine, S. 1987, *Galactic Dynamics* (Princeton: Princeton Univ. Press)
 Bromm, V., Coppi, P. S., & Larson, R. B. 2002, *ApJ*, 564, 23
 Bromm, V., Ferrara, A., Coppi, P. S., & Larson, R. B. 2001, *MNRAS*, 328, 969
 Bullock, J. S., Kolatt, T. S., Sigad, Y., Somerville, R. S., Kravtsov, A. V., Klypin, A. A., Primack, J. R., & Dekel, A. 2001, *MNRAS*, 321, 559
 Couchman, H. M. P., Thomas, P. A., & Pearce, F. R. 1995, *ApJ*, 452, 797
 Fuller, T. M., & Couchman, H. M. P. 2000, *ApJ*, 544, 6
 Galli, D., & Palla, F. 1998, *A&A*, 335, 403
 Glover, S. C. O., Savin, D. W., & Jappsen, A.-K. 2005, *ApJ*, submitted (astro-ph/0506221)
 Haiman, Z., Abel, T., & Rees, M. J. 2000, *ApJ*, 534, 11
 Hollenbach, D., & McKee, C. F. 1979, *ApJS*, 41, 555
 Hutchins, J. B. 1976, *ApJ*, 205, 103
 Lipovka, A., Núñez-López, R., & Avila-Reese, V. 2005, *MNRAS*, 361, 850
 Machacek, M. E., Bryan, G. L., & Abel, T. 2001, *ApJ*, 548, 509
 Mashchenko, S., & Sills, A. 2005a, *ApJ*, 619, 243
 ———. 2005b, *ApJ*, 619, 258
 Nagakura, T., & Omukai, K. 2005, *MNRAS*, 364, 1378
 Navarro, J. F., Frenk, C. S., & White, S. D. M. 1997, *ApJ*, 490, 493
 O’Shea, B. W., Abel, T., Whalen, D., & Norman, M. L. 2005, *ApJ*, 628, L5
 Peebles, P. J. E. 1984, *ApJ*, 277, 470
 Peebles, P. J. E., & Dicke, R. H. 1968, *ApJ*, 154, 891
 Ricotti, M., & Gnedin, N. Y. 2005, *ApJ*, 629, 259
 Ricotti, M., Gnedin, N. Y., & Shull, J. M. 2002, *ApJ*, 575, 49
 Spergel, D. N., et al. 2003, *ApJS*, 148, 175
 Tegmark, M., Silk, J., Rees, M. J., Blanchard, A., Abel, T., & Palla, F. 1997, *ApJ*, 474, 1
 Wishart, A. W. 1979, *MNRAS*, 187, 59P
 Yoshida, N., Abel, T., Hernquist, L., & Sugiyama, N. 2003, *ApJ*, 592, 645
 Zhao, D. H., Jing, Y. P., Mo, H. J., & Börner, G. 2003a, *ApJ*, 597, L9
 Zhao, D. H., Mo, H. J., Jing, Y. P., & Börner, G. 2003b, *MNRAS*, 339, 12